Research Square

Preprints are preliminary reports that have not undergone peer review.
They should not be considered conclusive, used to inform clinical practice,
or referenced by the media as validated information.

Unravelling the Descriptors of Intracrystalline Diffusion and Al Location on Hollow Zeolite Nanosheets for Target Acid-Base Co-Catalyzed Reaction

Zhe Hong

hongzhe@zjxu.edu.cn

Jiaxing University https://orcid.org/0000-0002-0974-5725

Lei Miao

Tongji University

Chuanfang Xiong

Jiaxing Ecological Environment Emergency Monitoring and Accident Investigation Center

Chao Gu

Jiaxing University

Na Li

Jiaxing University

Fangtao Huang

Tongji University

zhirong zhu

Tognji university

Lei Li

Jiaxing University https://orcid.org/0000-0003-4949-6484

Article

Keywords: Zeolites, Diffusion, Acid-base property, Al distribution, Side-chain alkylation

Posted Date: February 27th, 2026

DOI: https://doi.org/10.21203/rs.3.rs-8783288/v1

License: This work is licensed under a Creative Commons Attribution 4.0 International License. Read Full License

Additional Declarations: There is **NO** Competing Interest.

Abstract

Rational design of zeolites with improved diffusion properties and desirable acid-base densities is vital in relevant heterogeneous catalysis process. Herein, an effective protocol is developed to achieve the synchronous modulation of intracrystalline diffusion and Lewis acid-base sites distributions via constructing hollow zeolite nanosheets. We disclose the significant application of the desired catalyst in the reaction of toluene side-chain alkylation. The reaction results demonstrate that the platelike zeolite after alkali-treatment (CsZ5-U-AT) exhibits a higher toluene conversion (12.1%) and styrene selectivity (80.2%), accompanied by an extended catalytic stability (> 100 h) than conventional catalyst. Structure-performance relationships in side-chain alkylation are established for optimal catalyst in comparison with other catalysts using an experimentally derived descriptor that takes into account two critical physicochemical properties: mass transport and acid-base site densities. The explanations are as follows: (i) The hollow structure and short *b*-axis of desired catalysts synergistically facilitate the intracrystalline diffusivity, thereby improving the utilization of active sites; (ii) Partial framework Al sites are transformed to EFAL species (LASs) and “acid-free” $Al(OH)_4^-$ during alkali-treatment process, which modulating the Lewis acid-base sites; (iii) The Si-zoned external surface constructed during “desilication and recrystallization” process could improve shape-selective capability. In this case, the synchronous modulation of desirable intracrystalline diffusion and acid-base distributions can be achieved, and the ideal catalysts for acid-base catalyzed reactions can be designed.

1. Introduction

Zeolites, one of the typical crystalline microporous materials, are widely used in heterogeneous catalysis fields [1–2]. Of particular interest is the production of styrene, which is a valuable raw material in the production of fine chemicals and polymers [3]. Side-chain alkylation of toluene with methanol has been recognized as a potential one-step route, which could reduce the energy consumption in large scale styrene production and thus enable the mitigation of artificial CO_2 emission [4–6]. It was firstly reported that this green route can occur on alkali metal ion-exchanged FAU zeolites [7]. From then on, intensive study [8–10], including our previous work [11–15], has mainly focused on the rational design of alkali metal modified zeolite catalysts (especially Cs^+ exchanged zeolite) for this acid-base co-catalyzed reaction. Nevertheless, the modulation of Lewis acid-base pairs and diffusion limitation are the two key scientific issues.

The intracrystalline diffusional problems can be partially circumvented by reducing the path length through the zeolite crystal. Recently, the *b*-axis-oriented MFI zeolites have attracted extensive attention owing to their shortened *b*-axis, which provide a short diffusion path along straight channels [16]. It shows efficient catalytic performance in different catalytic process, such as the methanol-to-hydrocarbon (MTH) [17], methanol to propylene (MTP) [18], catalytic cracking [19], as well as other diffusion-restricted reactions [20]. Lately, we reported a Cs modified platelike ZSM-5 with ultrathin *b*-axis to enhance the mass transport and catalytic activity in side-chain alkylation reaction [21]. Constructing hollow structure within zeolites by alkali-treatment is another effective strategy to improve intracrystalline diffusivity. However, the effect of the alkali treatment process on acid-base distribution has not been sufficiently studied. Actually, the desilication would affect the acid and base densities because of the variation of bulk Si/Al ratio via alkali treatment [22, 48]. Li et al. unraveled the crucial roles of spatial Al distribution on modulating the Brönsted acid site (BAS) densities of hierarchical counterparts [23]. This inspiring work have provided guidelines designing ideal catalysts for acid-catalyzed reactions. Nevertheless,

synchronously achieving desirable intracrystalline diffusion and acid-base distributions during precise alkali-treatment is still challenging.

Herein, two MFI samples with different *b*-axis thickness are prepared and treated by TPAOH (see detailed synthesis conditions in **Supporting Information**). After Cs modification, the toluene side-chain alkylation performances of these catalysts are systematically compared. As the platelike sample after alkali-treatment (CsZ5-U-AT) exhibits superior catalytic performances, as well as extended catalytic stability, which is apparently related to its improved intracrystalline diffusivity bring by hollow structure and short *b*-axis. More importantly, we unravel the variation trends of Al distribution in zeolite during alkali-treatment process in determining the transform degree of framework tetrahedral Al, which precisely modulate the acid and base sites. Additionally, The Si-zoned external surface constructed during “desilication and recrystallization” process is observed to improve shape-selective capability. In this case, the artful alkali-treatment strategy of zeolites is proposed for achieving desirable intracrystalline diffusion and desirable acid-base densities, and the ideal catalysts for toluene side-chain alkylation and other acid-base catalyzed reactions can be designed.

2 Results and discussion

2.1 Resolving the Structure and Morphology

CsZ5-U and CsZ5-C samples with distinct *b*-axis thicknesses are synthesized via the hydrothermal process with or without moderate urea addition, respectively (Fig. 1a). Both Scanning electron microscopy (SEM) and transmission electron microscopy (TEM) images show that the samples of CsZ5-U and CsZ5-C have diverse morphology (Fig. 1b, 1d and **Figure S1**). The CsZ5-U exhibits a well-formed platelike morphology, while CsZ5-C exhibits a typical rounded-boat morphology. The distinct morphology can also be confirmed by high-angle annular dark-field (HAADF) images (Fig. 1f and **Figure S2**). Meanwhile, HAADF and EDS mapping images reveal that Si, O, Al and Cs elements are homogeneously distributed on the entire surface of both CsZ5-U and CsZ5-C zeolites (Fig. 1g and **Figure S3**). The thickness distribution indicate that the samples of CsZ5-U and CsZ5-C have the average *b*-axis thicknesses of 42 $\pm$ 3 and 100 $\pm$ 1 nm, respectively (Fig. 1i and **Figure S4a**). Atomic force microscopy (AFM) images also demonstrate that *b*-axis thickness of platelike CsZ5-U is ~ 45 nm (Fig. 1h, inset), which is nearly in accordance with the SEM results.

Then, CsZ5-U-AT and CsZ5-C-AT, treated by TPAOH solution, are carefully prepared. Clearly, hollow structures are formed in both two samples after alkali-treatment (Fig. 1c, 1e, 1j and **Figure S5**). Meanwhile, The HADDF and EDS mapping images of CsZ5-U-AT and CsZ5-C-AT are involved to display element distribution (Figs. 1l and **Figure S6**). SEM images indicate that the hollow zeolites maintain intact shells despite suffering the alkali treatment process (**Figure S7**). Interestingly, some small nanocrystals on the surface of ZSM-5 after alkali-treatment are observed. During the alkali-treatment process, TPA^+ ions are preferentially attached on the surface of ZSM-5 with $Si - O^-$ via electrostatic interactions. Simultaneously, the silicate oligomers are leached from the interior of the ZSM-5 crystal. Then, the leached silicate oligomers interact with TPA^+ aggregates on the ZSM-5 surface to form the silicate/TPA^+ intermediates, and recrystallize at 170 ^oC. Based on the mechanism of desilication and recrystallization, we infer that the Si-zoned surface are formed on the hollow-structured zeolite. Furthermore, the bulk Si/Al ratios of the two kinds of Cs-ZSM-5 slightly decrease after alkali-treatment, whereas the surface Si/Al ratio increase on the contrary (Table 1). The opposite variation trends for the bulk and surface Si/Al ratios after alkali-treatment is in accordance with the deduction of Si-zoned surface for hollow samples. The elaborate

structure of CsZ5-U-AT is further resolved by using integrated differential phase contrast (iDPC) STEM technique. In the iDPC-STEM images obtained from local structures, we can observe a representative MFI straight channel along the [010] axis (Fig. 1k). This confirms that the straight channel is perpendicular to the surface of the platelike hollow-structured zeolite.

In the X-ray diffraction (XRD) results, all catalysts exhibit typical characteristic peaks of MFI phase with sound crystallinity (**Figure S8**). Interestingly, the intensity ratio between 8.9° (010) and 7.9° (101) in the CsZ5-U is much higher than CsZ5-C, indicating the enhanced diffraction along (010) planes in platelike ZSM-5. This is the consequence of the shortened *b*-axis thicknesses and larger *c*-axis of CsZ5-U. However, there is a noticeable reduction in the (010)/(101) intensity ratio for the CsZ5-U after alkali-treatment, which should be ascribed to the presence of Si-zoned external surfaces after desilication and recrystallization, thereby leading to less diffraction along (010) orientation. The N_2 adsorption-desorption isotherms of all samples (including Na-type samples) are displayed in **Figure S9**. The type-I isotherms can be observed for CsZ5-C and CsZ5-U samples with fast uptake at low relative pressure, implying the typical microporous structure. After alkali treatment, CsZ5-C-AT and CsZ5-U-AT exhibit an additional hysteresis loop from P/P_0 = 0.50 to 0.99, indicating the formation of voids in the interior of zeolite crystals. Notably, the CsZ5-U-AT sample has a largest total volume (V_{micro}, 0.42 $cm^3\ g^{-1}$) and specific surface area (S_{BET}, 471 $m^2\ g^{-1}$) compared with other samples (Table 1), which should be brought by the synergistic effect of hollow structure and stacked platelike structure. This can enhance the accessibility of reactants to the acid and base sites of catalysts. Besides, textural properties and Si/Al ratio of different Na-type ZSM-5 samples exhibit the similar variation trends with the Cs^+-exchanged samples (**Table S1**).

Table 1
Textural properties, Si/Al ratio and Cs content of different Cs-ZSM-5 catalysts

Sample	S_{BET} [a] ($m^2\ g^{-1}$)	V_{micro} [b] ($cm^3\ g^{-1}$)	V_{total} [c] ($cm^3\ g^{-1}$)	Bulk Si/Al ratio [d]	Surface Si/Al ratio [e]	Cs content (wt %) [f]
CsZ5-C	369	0.18	0.20	25.8	26.2	12.2
CsZ5-U	456	0.21	0.31	25.4	25.2	13.1
CsZ5-C-AT	423	0.17	0.28	24.9	29.8	12.8
CsZ5-U-AT	471	0.19	0.42	24.3	30.1	13.4

[a] BET surface area calculated using BET method.

[b] Micropore volume calculated using *t*-plot method.

[c] Total pore volume calculated at p/p_0 = 0.99.

[d] Determined by XRF results.

[e] Calculated by XPS results.

[f] Determined by ICP-AES results.

2.2 Catalytic performance

The catalytic performances in toluene side-chain alkylation are evaluated over different catalysts (Fig. 2a-2b and **Figure S10**). Meanwhile, the reaction results in more detail are summarized in Table 2. The CsZ5-U catalyst, with a platelike architecture, exhibited improved catalytic performance in comparison with the conventional CsZ5-C catalyst, in terms of toluene conversion (10.9% vs 6.1%), styrene selectivity (54.8% vs 43.5%) and methanol utilization efficiency (40.2% vs 30.6%) under identical reaction conditions (430 ^{o}C, TOS = 1 h). After TPAOH treatment, a more inspiring catalytic behavior is exhibited. The optimal CsZ5-U-AT catalyst exhibits superior catalytic performance in comparison with other catalysts (including commercial Cs-ZSM-5 and other reference catalysts reported in literature, see **Table S2**), in terms of toluene conversion (12.1%), styrene selectivity (80.2%) and methanol utilization efficiency (47.8%). Notably, no side-chain alkylation product is observed on all Na-type ZSM-5 samples (**Figure S11**), indicating the necessity of Cs species for this reaction. In addition, the detailed gas product distribution from toluene-methanol reaction over different catalysts are provided in **Table S3**.

To further verify the intrinsic activity, we investigate the normalized styrene formation rates and the apparent activation energies (E_a). Before quantifying kinetic data, the transport effect and product inhibition effect are firstly excluded to ensure the accuracy of kinetic data (see details in **Figure S12** and **Figure S13**). Figure 2c confirms the styrene formation rates normalized by total Cs species, and the order are ranked as follows: CsZ5-U-AT > CsZ5-U > CsZ5-C-AT > CsZ5-C. To clarify the catalytic reaction data more comprehensively, the TOF values are also calculated via total Cs^+ and total base sites as active sites respectively. The results indicate that both the values of TOF_{Cs+} and TOF_{base} show the same order to that of TOF_{Cs} among these catalysts (**Figure S14** and Table 2). Furthermore, The E_a order is inverse to that of the normalized rates. Besides, the corresponding pre-exponential factors (A) are also analyzed (Table 2). The ranking order of A is the same as that of E_a order. These results are good agreements in the general perception that the lower E_a and corresponding A value is, the quicker reaction rate is. The CsZ5-U-AT catalyst achieves the highest TOF_{Cs} (0.559 $mmol_{ST}$ $molCs^{-1}$ h^{-1}) and the lowest E_a value (34 ± 1 kJ mol^{-1}), proving its distinguished intrinsic activity.

Curiously, CsZ5-U-AT could achieve significantly higher styrene selectivity than CsZ5-U although they all exhibit short *b*-axis thicknesses (Fig. 1i and **Figure S4c**). The Si-zoned external surface seems to be one of the reasons since it can eliminate external acid sites, thereby avoid the nonshape-selective side reactions. To verify this, the performance of a SiO_2 surface modified CsZ5-U catalyst (denoted as CsZ5-U-Si, see catalytic performance, TEM and HAADF-STEM images in **Figure S15** and **Figure S16**) is compared to those of CsZ5-U and CsZ5-U-AT. CsZ5-U-Si indeed exhibits a higher styrene selectivity (77.2%) than CsZ5-U (54.8%), but both toluene conversion and styrene selectivity are still not as good as CsZ5-U-AT. Hence, the critical factor responsible for the superior performance of CsZ5-U-AT should be deeply studied.

Table 2
Catalytic performances over different Cs-ZSM-5 catalysts to produce styrene.

Sample	Toluene conversion (%) [a]	Product Selectivity (%)			Normalized rates			E_a (kJ/mol)	ln (A)
		Styrene	Ethylbenzene	Others [b]	TOF_{Cs} [c]	TOF_{Cs+} [d]	TOF_{base} [e]		
CsZ5-C	6.1	43.5	38.6	17.9	0.168	0.358	0.102	63±2	9.1
CsZ5-C-AT	8.0	66.7	23.1	10.2	0.314	0.650	0.187	55±2	8.2
CsZ5-U	10.9	54.8	31.0	14.2	0.361	0.634	0.192	48±1	7.2
CsZ5-U-AT	12.1	80.2	13.3	6.5	0.559	0.901	0.294	34±1	5.3

Reaction conditions: 430 ^{o}C, toluene/methanol ratio = 3.0, WHSV = 2.0 h^{-1}.

[a] Determined at 1 h time-on-stream.

[b] Major byproducts are ring alkylation products, including benzene, xylenes, trimethylbenzene and methyl-ethylbenzene.

[c] Determined by normalization of total number of Cs sites (unit $mmol_{styrene}\ mol_{Cs}^{-1}\ h^{-1}$).

[d] Determined by normalization of Cs^+ sites (unit $mmol_{styrene}\ mol_{Cs+}^{-1}\ h^{-1}$).

[e] Determined by normalization of total base sites (unit $mmol_{styrene}\ mol_{basicity}^{-1}\ s^{-1}$) ($\times 10^{-2}$).

2.3 Improvement of Intracrystalline Diffusivity

In general, the different diffusion behaviors arising from morphology distinction would affect the catalytic performance. Thus, the variation trends in the diffusion behaviors are elucidated by using intelligent gravimetric analyzer (IGA) technique. The diffusion time constant (D_{eff}/L^2) is a proxy for the diffusion resistance [24–25]. Generally, the higher value of D_{eff}/L^2 means the faster intracrystalline diffusion rate and weaker diffusion resistance in zeolite pore systems [26–27]. Toluene with a comparable kinetic diameter as the micropore sizes of MFI zeolite is used as the probe molecule to elucidate the diffusion behaviors of different samples based on Fick's second law. The D_{eff}/L^2 value, deduced from the slope, is increased with the TPAOH treatment for both CsZ5-C and CsZ5-U as incremental voids are introduced (Fig. 3a and 3b). On the other hand, The D_{eff}/L^2 value of platelike sample ($2.32 \times 10^{-3}\ s^{-1}$ for CsZ5-U) is substantially higher than the rounded-boat sample ($7.96 \times 10^{-4}\ s^{-1}$ for CsZ5-C). It indicates that the shorter *b*-axis thicknesses also lead to the faster diffusion rates. The understanding of the relationship between the catalysis and the diffusion behavior is crucial to future catalyst design for industrial catalysis. Thereby, we establish the relationship between D_{eff}/L^2 and reaction activities. The catalytic properties, expressed by the toluene conversions and styrene formation rates, are correlated with the diffusive rates of toluene over different catalysts (Fig. 3c). Clearly, both the toluene conversions and styrene

formation rates gradually increase with the increasing D_{eff}/ L^2 values, indicating the pivotal role of diffusivity in the reaction of toluene side-chain alkylation. Additionally, The D_{eff}/L^2 increases non-linearly with the shortening of *b*-axis thickness over different samples, confirming that the platelike morphology of MFI zeolite could facilitate the intracrystalline diffusion of reactants (Fig. 3d).

2.4 Distinct effects on zeolite acid-base properties

The desilication via TPAOH treatment would not only affect the diffusion behaviors but also the acid-base properties, thereby playing a significant role in this acid-base co-catalyzed reaction. Firstly, the CO_2-TPD results show that the base strength decreases, whereas the amounts of base sites increase from CsZ5-C to CsZ5-U (Fig. 4a). After alkali-treatment, the base amount of both CsZ5-C-AT and CsZ5-U-AT slightly increase. Notably, the strong acid amount of both CsZ5-C-AT and CsZ5-U-AT obviously increase comparing with parent CsZ5-C and CsZ5-U, respectively (Fig. 4b and **Table S4**). Especially for CsZ5-U-AT, which almost represents the disappeared strong acid sites (> 300°C), even though it has a lower bulk Si/Al ratio of 24.3 than CsZ5-U. It means that partial nature of acid sites is changed because of alkali treatment. Hence, the nature of acid sites is further elucidated by using pyridines (Py) and carbon monoxides (CO) adsorbed FTIR spectra. In Py adsorbed FTIR spectra, the band at 1545 cm^{-1} could be assigned to pyridines-Brønsted acid sites (BASs) interaction, while the bands at 1455 cm^{-1} could be ascribed to pyridines-Lewis acid sites (LASs) interaction [28]. The ratio of BASs concentrations to LASs concentrations (B/L) in alkali-treated samples to that in pristine samples are compiled. Clearly, the B/L on alkali-treated CsZ5-C-AT (0.32) and CsZ5-U-AT (0.19) decreases compared with pristine CsZ5-C (0.34) and CsZ5-U (0.24), respectively (**Table S4**). Meanwhile, CO adsorbed FTIR provides a consistent trend of variations in the distribution of acid sites among these catalysts before and after alkali treatment (Fig. 4d and **Figure S17**). It can be concluded that partial BASs are lost whereas some new LASs are created during alkali treatment process. In addition, the platelike CsZ5-U has more LASs than CsZ5-C, which might be due to that unexpected N species introduction induces the restructuring of Lewis pairs on platelike zeolite. This subject has been deeply discussed in our previous work [29].

On the other hand, the external acid sites are characterized by FTIR spectra using 2,6-di-tert-butylpyridine (DTBPy) as the probe molecule, which is too large to enter the 10 member-ring (10 MR) channels of zeolites. The band at ~ 3368 cm^{-1} assigning to the adsorbed $DTBPyH^+$ ions, is used to monitor the surface BASs. As shown in Fig. 4e, the intensities of the band at 3368 cm^{-1} for pristine samples are greater than those for corresponding alkali-treated samples. Especially for the very weak peak at 3368 cm^{-1} on CsZ5-U-AT means few external acid sites, attributing to the inert Si-zoned external surface after alkali treatment [14, 29, 30] (see **Figure S7** and Table 1). The weaker external acidity in alkali-treated samples is also confirmed by the catalytic cracking of bulky triisopropylbenzene (TIPB, kinetic diameter ~ 0.85 nm). As shown in Fig. 4f, the conversion of TIPB is 25.4% and 20.5% for CsZ5-U and CsZ5-U-AT catalysts, respectively, likewise implying the inert external surface of CsZ5-U-AT.

2.5 Descriptor of Al sites distribution and coordination environment

In general, for the MFI zeolites with uniformly distributed Al sites, the Al structure would be homogeneously damaged when adjacent Si sites are removed during alkali treatment process, ultimately leading to a lower B/L

ratio [23]. We reasonably believe that the variation in acid-base nature should be attributed to the restructuring of Al location, which is induced by alkali treatment. For further demonstration, the spatial Al distribution and coordination environment are deeply studied. First, the ^{1}H magic-angle spinning (MAS) nuclear magnetic resonance (NMR) spectra indicate that the signals at 1.7 ppm belongs to the isolated silanol groups (Si – OH) or geminal Si – OH groups, while the signal at 2.8 ppm can be assigned to the aluminium hydroxyl (Al – OH) species [31] (Fig. 5a and 5b). Besides, the peaks at 3.9 and 5.9 ppm can be associated with bridged hydroxyl species (Si(OH)Al, free BAS or hydrogen-bonded BAS) and hydrogen-bonded Si – OH defects, respectively [32]. Notably, for both CsZ5-C and CsZ5-U, the intensity of the peaks at 2.8 ppm increases whereas the peaks at 3.9 ppm are clearly suppressed after alkali treatment. This variation should be associated with the changes of Al sites in zeolite.

To verify Al sites in terms of their coordination, the ^{27}Al MAS NMR is further performed. Figure 5c and 5d indicate that both CsZ5-C and CsZ5-U have dominant tetrahedral Al sites (60 ppm region) but few octahedral Al sites (0 ppm region). Interestingly, the octahedral Al sites obviously appear in alkali-treated catalysts (CsZ5-C-AT and CsZ5-U-AT). Simultaneously, the peak belonging to tetrahedral Al sites decreases and a broader peak extending to the lower chemical shift (~ 58 ppm) is observed on alkali-treated catalysts, suggesting the possible generation of distorted tetrahedral Al sites [33]. Combined with the ^{27}Al Multiple Quantum (MQ) MAS NMR spectra of CsZ5-U and CsZ5-U-AT, we can further verify the formation of extra-framework Al sites after alkali treatment, including octahedral Al sites and distorted tetrahedral Al sites (Fig. 5e and 5f).

The obvious reduction in peak intensity at 60 ppm (^{27}Al MAS NMR) of the alkali-treated catalysts indicate that some tetrahedral Al sites must be transformed into other Al species during the “dissolution-recrystallization” process. The intensify of the ^{1}H NMR signals at 2.8 ppm and ^{27}Al MAS NMR signals at 0 ppm indicates the formation of extra-framework Al (EFAL) species. Moreover, the decreasing of the ^{1}H NMR signals at 3.9 ppm and broader peak of ^{27}Al MAS NMR signals at ~ 58 ppm implies that some of NMR invisible Al species may appear. Recently, Xu et al. assigned the broader signal of ^{27}Al MAS NMR signals to “acid-free” Al sites [23]. Inspiringly, in this work, the framework Al should be partially transformed into re-deposited $Al(OH)_4^-$ in the TPAOH solution during alkali treatment process, and then transformed into Al_{IV}-OH defects and NMR-invisible Al_xO_y clusters in succession after drying and calcination because of the large quadrupole coupling constant (QCC). Based on the above discussion, we demonstrate how distinct distribution of Al sites among these catalysts resulted in distinct nature of acid sites. During alkali-treatment process, a part of framework Al fell off and transformed to EFAL species, which act as surface LASs [13]. Meanwhile, some of framework Al migrated around the Si-OH in zeolite as $Al(OH)_4^-$, which contribute negligibly to both BAS and LAS.

On the other hand, considering the necessity of Cs species for toluene side-chain alkylation reaction (see details in **Figure S11**), the nature of Cs species is further studied. The Cs $3d_{5/2}$ XPS spectra show that all the samples display two peaks, which attribute to cesium ions (~ 721.9 eV) balancing the negative charge of zeolite framework and cesium oxides (~ 722.8 eV) depositing on zeolite, respectively [34] (Fig. 6a and 6b). The proportion of Cs^+ increases in the order of CsZ5-C < CsZ5-C-AT < CsZ5-U < CsZ5-U-AT. Interestingly, the platelike samples (CsZ5-U and CsZ5-U-AT) show significantly more Cs^+ than other two samples. Furthermore, the coordination environment of Cs species is explored by the X-ray absorption near-edge structure (XANES) at Cs L_3-edge (Fig. 6c). Compared to CsZ5-C and Cs_2CO_3 standard sample, CsZ5-U-AT exhibits a decreased absorption energy,

implying a lower oxidation state of Cs species in CsZ5-U-AT. This result aligns with the Cs $3d_{5/2}$ XPS results. Notably, compared with CsZ5-C, CsZ5-U-AT shows an obvious increase in white line intensity. The white line peak intensity in the XANES spectra at Cs L_3-edge reflects the multielectron photoexcitation feature and the larger intensity for CsZ5-U-AT implies the local arrangement around Cs^+ site and more active Cs^+ single sites in ZSM-5-zeolite channels [35]. The coordination structure of optimal catalyst and control sample is also investigated by EXAFS spectra (Fig. 6d, **Figure S18** and **Table S5**). The CsZ5-U-AT showed a bonding distance of 3.86, suggesting the formation of Cs-O-Si (Al) coordination shell [36–37].

Based on above discussion combining reaction results and catalyst characterizations, we conclude that the distinct catalytic performance among these catalysts is predominantly attributed to the variation in diffusion behaviors and Al site locations before and after alkali treatment. The explanations are as follows: (i) The hollow structure and short *b*-axis of desired catalysts synergistically facilitate the intracrystalline diffusivity, thereby improving the utilization of active sites on catalysts; (ii) Partial framework Al sites are transformed to EFAL species (LASs) and “acid-free” $Al(OH)_4^-$ during alkali-treatment process, this precise modulation on Lewis pairs boost the catalytic activity of target acid-base co-catalyzed reaction; (iii) The Si-zoned external surface constructed during “desilication and recrystallization” process could improve shape-selective capability, thereby resulting in high styrene selectivity.

2.6 Stability and deactivation mechanism

Another observation is the excellent catalytic stability of desired catalyst in the long-time test. The toluene conversion and styrene selectivity on CsZ5-U-AT only show 1.4% and 3.7% drops respectively after 100 h reaction (Fig. 7b). Differently, the toluene conversion on CsZ5-C quickly decreases from 6.3% to 2.2% (4.1% drops) and the styrene selectivity decreases from 43.9% to 33.2% (10.7% drops) after 100 h reaction (Fig. 7a). In the long-time reaction, formation of coke is deemed as the major cause for catalyst deactivation. Hence, the quantity and nature of coke species are monitored during side-chain alkylation reaction by using various characterization methods. Firstly, TG curves reveal that the coke loss on spent CsZ5-U-AT is lower than spent CsZ5-C catalyst (4.3% vs 8.1%), implying the better coke resistance of the former (Fig. 7c and **Table S6**). Subsequently, The GC-MS chromatograms results indicate that polymethylbenzenes, polymethylnaphthalenes and naphthalene are the major organic species in spent catalysts. Notably, it is evident that more bulkier coke species are detected in spent CsZ5-C than that of CsZ5-U-AT, giving another piece of evidence about the excellent anti-coke ability of CsZ5-U-AT (**Figure. S19**). To track the spatiotemporal progression of coke species in the zeolite crystals, the reactions are repeated using the operando ultraviolet-visible light (UV-vis) diffuse reflectance spectroscopy coupled with online gas chromatography. Generally, a UV-vis spectrum obtained can be grouped into three regions, including HCP species, internal coke and external coke [38–39]. The operando UV-vis spectra show nearly equivalent HCP species and internal coke between CsZ5-C and CsZ5-U-AT catalysts. However, there is an obvious reduction in the quantity of external coke on CsZ5-U-AT catalyst (Fig. 7d-7f and **Figure S20**). This is attributed to the presence of ultrathin *b*-axis and hollow structure which leads to enhanced mass transport and reduced residence time, thereby suppressing the accumulation of bulkier coke species at the pore mouths. Therefore, the extended catalytic stability is achieved upon the CsZ5-U-AT catalyst. Besides, the N_2 adsorption isotherms of spent catalysts are measured to indicate the pore blockage by coke species (**Figure. S21** and **Table S7**).

2.7 Reaction mechanism

To gain insights into the key intermediate and reaction pathway for the synthesis of styrene, we further implement time-dependent *in situ* DRIFTS measurements under methanol feed at 430 ^{o}C. As shown in *in situ* DRIFT spectra over CsZ5-U-AT, the peak at 1372 cm^{-1} appearing at initial 2 min is attributed to the methoxy (CH_3O*) species (Fig. 8a) [40]. Almost simultaneously, a distinct peak at 1595 cm^{-1} assigning to formates (HCOO*) species is detected [41–42], which has been regarded as the key reactive intermediate in the reaction of side-chain alkylation of toluene [11, 43]. It infers that the HCOO* generated from dehydrogenation of CH_3O* is an extremely rapid process. Both the peaks of CH_3O* and HCOO* species gradually intensify with the reaction time and nearly reach equilibrium at 60 min on the surface of CsZ5-U-AT. Meanwhile, the peaks for surface CH_3O* and HCOO* species with the C–H symmetric and asymmetric stretching vibrations are clearly visible at 2808/2926 cm^{-1} and 2865/3010 cm^{-1}, respectively (Fig. 8b) [44–45]. Besides, the weak peaks at 1053, 1142 and 2742 cm^{-1} are attributed to the unidentate or bidentate carbonates, which might be produced by dehydrogenation of formates or adsorbed CO_2* [46–47]. According to these evidences, the reaction routes are presumed to proceed as follows: (i) CH_3OH adsorbed on the Lewis sites of CsZ5-U-AT, and then successively dehydrogenate to produce CH_3O* and HCOO* intermediates (inverse formate reaction pathway); (ii) The derived HCOO* intermediates react with polarized toluene via aldol type condensation (C-C bond coupling) to form styrene. *In situ* DRIFT spectra for CsZ5-C exhibits similar characteristic bands but vastly different intensity of peaks. Importantly, the intensity of the key intermediates of HCOO* species over CsZ5-C are much lower than that over CsZ5-U-AT (Fig. 8c, 8d). Furthermore, The CsZ5-U-AT exhibits much higher HCOO*/CH_3O* ratio than that of CsZ5-C (**Figure S22**). It implies that reactive HCOO* is unstable, which may be consumed through reverse reaction with H* to regenerate CH_3O* on CsZ5-C. For CsZ5-U-AT, the modulated surface Lewis pairs and improved diffusion rates enhances CH_3OH activation, simultaneously suppresses HCOO* hydrogenation, thus facilitating the formation of more HCOO* intermediates.

3 Conclusions

In this study, two MFI samples with different *b*-axis thickness are prepared via urea-assisted crystallization strategy and then treated by TPAOH, achieving the synchronous modulation of intracrystalline diffusion and acid-base distributions. Subsequently, the catalytic performances of these samples in the toluene side-chain alkylation reaction are investigated. Among them, the platelike sample after alkali-treatment (CsZ5-U-AT) is nearly optimal, characterized by higher toluene conversion (12.1%), styrene selectivity (80.2%), accompanied by an extended catalytic stability (> 100 h). Furthermore, the CsZ5-U-AT achieves superior intrinsic activity, including higher styrene formation rates of 0.559 $mmol_{ST}$ $molCs^{-1}$ h^{-1} and lower E_a of 34 ± 1 kJ mol^{-1}. By tracking these catalysts before and after alkali-treatment through multiple characterization methods, we conclude that the distinct catalytic performance is predominantly attributed to the variation in diffusion behaviors and Al site locations before and after alkali treatment. The explanations are as follows: (i) The hollow structure and short *b*-axis of desired catalysts synergistically facilitate the intracrystalline diffusivity, thereby improving the utilization of Lewis acid-base sites and anti-coke capacity; (ii) Partial framework Al sites are transformed to EFAL species (LASs) and “acid-free” $Al(OH)_4^-$ during alkali-treatment process, which could modulate the desirable BAS and LAS densities, thus boosting the activity of target reaction; (iii) The Si-zoned external surface constructed during “desilication and recrystallization” process could improve shape-selective capability, resulting in high selectivity of product. Additionally, *in situ* DRIFTS results indicate that the modulated Lewis acid-base sites and improved

intracrystalline diffusion rates could enhance CH_3OH activation, simultaneously suppresses HCOO* hydrogenation, thus facilitating the formation of more key intermediates of HCOO*.

Declarations

Acknowledgements

The work described above was supported by the National Natural Science Foundation of China (22278175), Zhejiang Provincial Natural Science Foundation of China (ZCLQN25B0303) and Jiaxing City Public Welfare Research Project of China (2024AY10024). The authors gratefully acknowledge the support from Guangzhou Institute for Food Inspection (Doctoral Workstation of Guangdong Province). We also thank the researchers in the SCI-GO (www.sci-go.com) for their helping with AFM analysis.

References

1. Zhang MC, Zhong CQ, Wu HF, Yan X, Yan SY, Han JF, Wang X, Liu JX, Ren LM (2025) Silanol Nest Engineering Facilitates Migration-Driven Trapping of Strong Lewis Acid Sites in Self-Pillared Zeolites. Inorg Chem 64(33):17045–17057
2. Misaki S, Takabatake M, Hasegawa S, Manaka Y, Chun W-J, Motokura K (2024) Effect of zeolites on the alkylation of aromatics with alkanes using a Pd nanoparticle/solid acid cooperative catalytic system. Green Carbon 2(3):282–290
3. Vaughan BA, Webster-Gardiner MS, Cundari TR, Gunnoe TB (2015) A rhodium catalyst for single-step styrene production from benzene and ethylene. Science 348(6233):421–424
4. Hong Z, Xiong CF, Zhao GQ, Zhu ZR (2019) Side-chain alkylation of toluene with methanol to produce styrene: an overview. Catal Sci Technol 9(24):6828–6840
5. Ma QL, Cheng JN, Wu XJ, Xie J, Zhang RH, Mao ZH, Yang HF, Fan WJ, Zeng JR, Bitter JH, Li GN, Li ZL, Li C (2025) C-C bond coupling with sp3 C-H bond via active intermediates from CO_2 hydrogenation. Nat Commun 16(1):140–152
6. Chen SY, Liang ZW, Feng ZD, Feng ZC, Tang S, Li ZL, Wang JJ, Li C (2025) Hydrogenation of CO_2 to Propylene and Butene Over $ZnZrO_x$/SAPO-18. Angewandte Chemie-International Ed 64 (46), e202512845
7. Sidorenko YN, Galich PN, Gutirya VS (1967) Condensation of toluene and methanol upon synthetic zeolites containing ionexchange cations of alkali metals. Dokl Akad Nauk SSSR 173:132–133
8. Li PD, Han Q, Zhang XM, Yuan YY, Zhang YF, Guo HC, Xu L, Xu L (2018) A new insight into the reaction behaviors of side-chain alkylation of toluene with methanol over CsX. Catal Sci Technol 8(13):3346–3356
9. Cheng M, Wang Y, Wang WH, Wang GW, Zhu XL, Li CY (2021) Promoting effect of copper oxide on CsX zeolite catalyst for side-chain alkylation of toluene with methanol. Microporous Mesoporous Mater 311:110732
10. Ran ZZ, Liu JF, Mushtaq MA, Ji SF (2024) Preparation of Cs/CuAl-LDO@Al_2O_3@Fe_3O_4 magnetic catalysts and reaction mechanism of the side-chain alkylation of toluene to styrene. Catal Today 439:114771
11. Hong Z, Xiong CF, Wang X, Huang FT, Li L, Zhu ZR (2023) Ammonia pools effect in Cs modified X zeolites for side-chain alkylation of toluene with methanol. Chem Eng J 474:145650

12. Hong Z, Li L, Miao L, Zhao GQ, Zhu ZR (2023) Opening sodalite cages of X zeolite for boosting toluene side-chain alkylation performance. Catal Sci Technol 13(7):1991–1995
13. Hong Z, Wang X, Fang YS, Deng LH, Li L, Zhu ZR (2024) Restructuring Surface Lewis Pairs of FAU Zeolite through N Doping for Boosting the Toluene Side-Chain Alkylation Performance. Inorg Chem 63(7):3258–3266
14. Hong Z, Deng LH, Wang FL, Zhu FY, Fang YS, Song L, Li L, Zhu ZR (2024) Intergrowth MFI Zeolite with Inverse Al Zoning and Predominant Sinusoidal Channels for Highly Selective Production of Styrene. Inorg Chem 63(43):20888–20899
15. Hong Z, Zhao GQ, Huang FT, Wang XX, Zhu ZR (2022) Enhancing the side-chain alkylation of toluene with methanol to styrene over the Cs-modified X zeolite by the assistance of basic picoline as a co-catalyst. Green Energy Environ 7(6):1241–1252
16. Dai WJ, Kouvatas C, Tai WS, Wu GJ, Guan NJ, Li LD, Valtchev V (2021) Platelike MFI Crystals with Controlled Crystal Faces Aspect Ratio. J Am Chem Soc 143(4):1993–2004
17. Choi M, Na K, Kim J, Sakamoto Y, Terasaki O, Ryoo R (2009) Stable single-unit-cell nanosheets of zeolite MFI as active and long-lived catalysts. Nature 461(7261):246–U120
18. Sun Y, Cao SW, Wang J, Tang H, Yang ZK, Ma T, Gong YJ, Mo G, Li ZH (2022) Fabrication of Twin-Free Nanoslab ZSM-5 Zeolite with b-Axis Orientation for Super MTP Catalyst. ACS Sustain Chem Eng 10(29):9431–9442
19. Zhang JX, Ren LM, Zhou AJ, Li WH, Shang SJ, Liu Y, Jia ZH, Liu W, Zhang AF, Guo XW, Song CS (2022) Tailored Synthesis of ZSM-5 Nanosheets with Controllable b-Axis Thickness and Aspect Ratio: Strategy and Growth Mechanism. Chem Mater 34(7):3217–3226
20. Li H, Yu JY, Du K, Li WY, Ding L, Chen W, Xie SH, Zhang YH, Tang Y (2024) Synthesis of ZSM-5 Zeolite Nanosheets with Tunable Silanol Nest Contents across an Ultra-wide pH Range and Their Catalytic Validation. Angewandte Chemie-International Ed 63(24):202405092
21. Hong Z, Miao L, Deng L, Gu C, Gao Y, Xu Z, Zhu Z (2025) b-Axis oriented platelike MFI zeolite for efficient production of styrene: Synergy of diffusion anisotropy and Lewis pairs modulation. Chem Eng J 520:165870
22. Liao YH, Zhong RY, d'Halluin M, Verboekend D, Sels BF (2020) Aromatics Production from Lignocellulosic Biomass: Shape Selective Dealkylation of Lignin-Derived Phenolics over Hierarchical ZSM-5. ACS Sustain Chem Eng 8(23):8713–8722
23. Li JJ, Chen HH, Liu W, Zhi YC, Ta N, Xie SJ, Xu LY, Li XJ, Zhu XX, Xu ST (2025) Unravelling the Crucial of Spatial Al Distribution to Realize Precise Alkali-Treatment for Target Acid-Catalyzed Reactions. Angewandte Chemie-International Ed 64(4):202416564
24. Gao MB, Li H, Yang M, Gao SS, Wu PF, Tian P, Xu ST, Ye M, Liu ZM (2019) Direct quantification of surface barriers for mass transfer in nanoporous crystalline materials. Commun Chem 2:43–53
25. Chmelik C, Kärger J (2010) In situ study on molecular diffusion phenomena in nanoporous catalytic solids. Chem Soc Rev 39(12):4864–4884
26. Liu XL, Shi J, Yang G, Zhou J, Wang CM, Teng JW, Wang YD, Xie ZK (2021) A diffusion anisotropy descriptor links morphology effects of H-ZSM-5 zeolites to their catalytic cracking performance. Commun Chem 4(1):107–117
27. Vattipalli V, Qi XD, Dauenhauer PJ, Fan W (2016) Long Walks in Hierarchical Porous Materials due to Combined Surface and Configurational Diffusion. Chem Mater 28(21):7852–7863

28. Wang HQ, Shen BY, Chen X, Xiong H, Wang HM, Song WL, Cui CJ, Wei F, Qian WZ (2022) Modulating inherent lewis acidity at the intergrowth interface of mortise-tenon zeolite catalyst. Nat Commun 13(1):2924–2933
29. Jiao Y, Forster L, Xu S, Chen H, Han J, Liu X, Zhou Y, Liu J, Zhang J, Yu J, D'Agostino C, Fan X (2020) Creation of Al-Enriched Mesoporous ZSM-5 Nanoboxes with High Catalytic Activity: Converting Tetrahedral Extra-Framework Al into Framework Sites by Post Treatment. Angewandte Chemie-International Ed 59(44):19478–19486
30. Jiao F, Yu PY, Cui YC, Li H, Hu Q, Xu YA, Mintova S, Guo HL, Du HB (2023) Hollow STW-Type Zeolite Single Crystals with Aluminum Gradient for Highly Selective Production of p-Xylene from Methanol-Toluene Alkylation. Angewandte Chemie-International Ed 62(41):202310419
31. Schroeder C, Siozios V, Mück-Lichtenfeld C, Hunger M, Hansen MR, Koller H (2020) Hydrogen Bond Formation of Bronsted Acid Sites in Zeolites. Chem Mater 32(4):1564–1574
32. Schroeder C, Siozios V, Hunger M, Hansen MR, Koller H (2020) Disentangling Brønsted Acid Sites and Hydrogen-Bonded Silanol Groups in High-Silica Zeolite H-ZSM-5. J Phys Chem C 124(42):23380–23386
33. Chen KZ, Horstmeier S, Nguyen VT, Wang B, Crossley SP, Pham T, Gan ZH, Hung I, White JL (2020) Structure and Catalytic Characterization of a Second Framework Al(IV) Site in Zeolite Catalysts Revealed by NMR at 35.2 T. J Am Chem Soc 142(16):7514–7523
34. Ma QL, Cheng JN, Wu XJ, Xie J, Zhang RH, Mao ZH, Yang HF, Fan WJ, Zeng JR, Bitter JH, Li GN, Li ZL, Li C (2025) C-C bond coupling with sp^3 C-H bond via active intermediates from CO_2 hydrogenation. Nat Commun 16(1):140–152
35. Ghosh S, Acharyya SS, Yoshida Y, Kaneko T, Iwasawa Y, Sasaki T (2022) Nontraditional Aldol Condensation Performance of Highly Efficient and Reusable Cs^+ Single Sites in β-Zeolite Channels. ACS Appl Mater Interfaces 14(16):18464–18475
36. Park M, Kim S, Takahashi Y, Jeong HY (2022) Thermal stabilization of extraframework Cs^+ in zeolite 13X. J Nucl Mater 572:154078
37. Fan QH, Yamaguchi N, Tanaka M, Tsukada H, Takahashi Y (2014) Relationship between the adsorption species of cesium and radiocesium interception potential in soils and minerals: an EXAFS study. J Environ Radioact 138:92–100
38. Le TT, Qin W, Agarwal A, Nikolopoulos N, Fu DL, Patton MD, Weiland C, Bare SR, Palmer JC, Weckhuysen BM, Rimer JD (2023) Elemental zoning enhances mass transport in zeolite catalysts for methanol to hydrocarbons. Nat Catal 6(3):254–270
39. Dai H, Shen YF, Yang TM, Lee CS, Fu DL, Agarwal A, Le TT, Tsapatsis M, Palmer JC, Weckhuysen BM, Dauenhauer PJ, Zou XD, Rimer JD (2020) Finned zeolite catalysts. Nat Mater 19(10):1074–1083
40. Yan BH, Zhao BH, Kattel S, Wu QY, Yao SY, Su D, Chen JGG (2019) Tuning CO_2 hydrogenation selectivity via metal-oxide interfacial sites. J Catal 374:60–71
41. Liu XL, Wang MH, Zhou C, Zhou W, Cheng K, Kang JC, Zhang QH, Deng WP, Wang Y (2018) Selective transformation of carbon dioxide into lower olefins with a bifunctional catalyst composed of $ZnGa_2O_4$ and SAPO-34. Chem Commun 54(2):140–143
42. Lai YJ, Hong B, Zhou W, Wen DL, Xie YF, Luo F, Ye LM, Zuo JC, Yuan YZ (2024) Upgrading Trimethylbenzene to Durene by CO_2-Mediated Methylation over Cu-Boosted $ZnZrO_x$ Integrated with HZSM-5. ACS Catal 14(15):11780–11793

43. Lin D, Zhao HM, Zhang XY, Lan DX, Chun Y (2012) Formation and Function of Formate in the Side-Chain Alkylation of Toluene with Methanol. Chin J Catal 33(6):1041–1047
44. Wang S, Zhang L, Wang PF, Jiao WY, Qin ZF, Dong M, Wang JG, Olsbye U, Fan WB (2022) Highly selective hydrogenation of CO_2 to propane over $GaZrO_x$/H-SSZ-13 composite. Nat Catal 5(11):1038–1050
45. Yang Y, Mims CA, Mei DH, Peden CHF, Campbell CT (2013) Mechanistic studies of methanol synthesis over Cu from $CO/CO_2/H_2/H_2O$ mixtures: The source of C in methanol and the role of water. J Catal 298:10–17
46. Wang H, Fan S, Guo SJ, Wang S, Qin ZF, Dong M, Zhu HQ, Fan WB, Wang JG (2023) Selective conversion of CO_2 to isobutane-enriched C_4 alkanes over $InZrO_x$-Beta composite catalyst. Nat Commun 14(1):2627–2641
47. Wang YH, Kattel S, Gao WG, Li KZ, Liu P, Chen JGG, Wang H (2019) Exploring the ternary interactions in Cu-ZnO-ZrO_2 catalysts for efficient CO_2 hydrogenation to methanol. Nat Commun 10:1166–1176
48. Li Y, Liu X, Zhang K, Zhao S, Wu L, Guo Q, Du H, Wang F (2024) One-pot conversion of cellulosic sugars into methyl lactate using hierarchical Sn-MFI zeolite with intracrystalline mesoporosity. Green Carbon 2(4):383–392

Figures

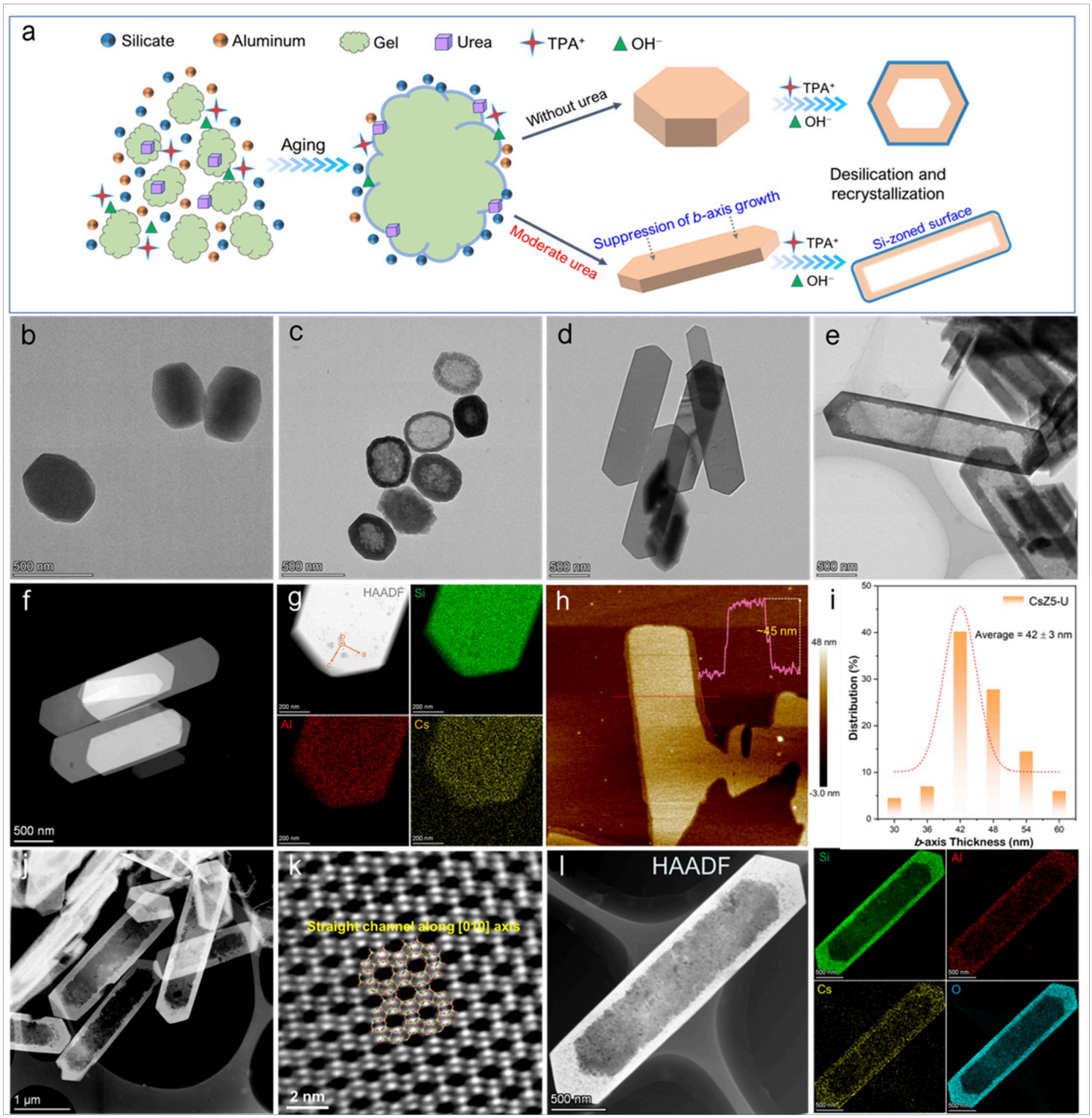


Figure 1

General structure features of different Cs-ZSM-5 catalysts. (a) Schematic illustration of the synthesis strategy; (b-e) TEM images to reveal different *b*-axis thickness and hollow structure after alkali-treatment: (b) CsZ5-C, (c) CsZ5-C-AT, (d) CsZ5-U, (e) CsZ5-U-AT; (f) HAADF-STEM images of CsZ5-U; (g) HAADF and EDS mapping images of CsZ5-U; (h) AFM images and (i) thickness distribution along *b*-axis of CsZ5-U (determined by statistics of 100 specimens in SEM images); (j) HAADF-STEM images and (k) iDPC-STEM images of CsZ5-U-AT; (l) HAADF and EDS mapping images of CsZ5-U-AT.

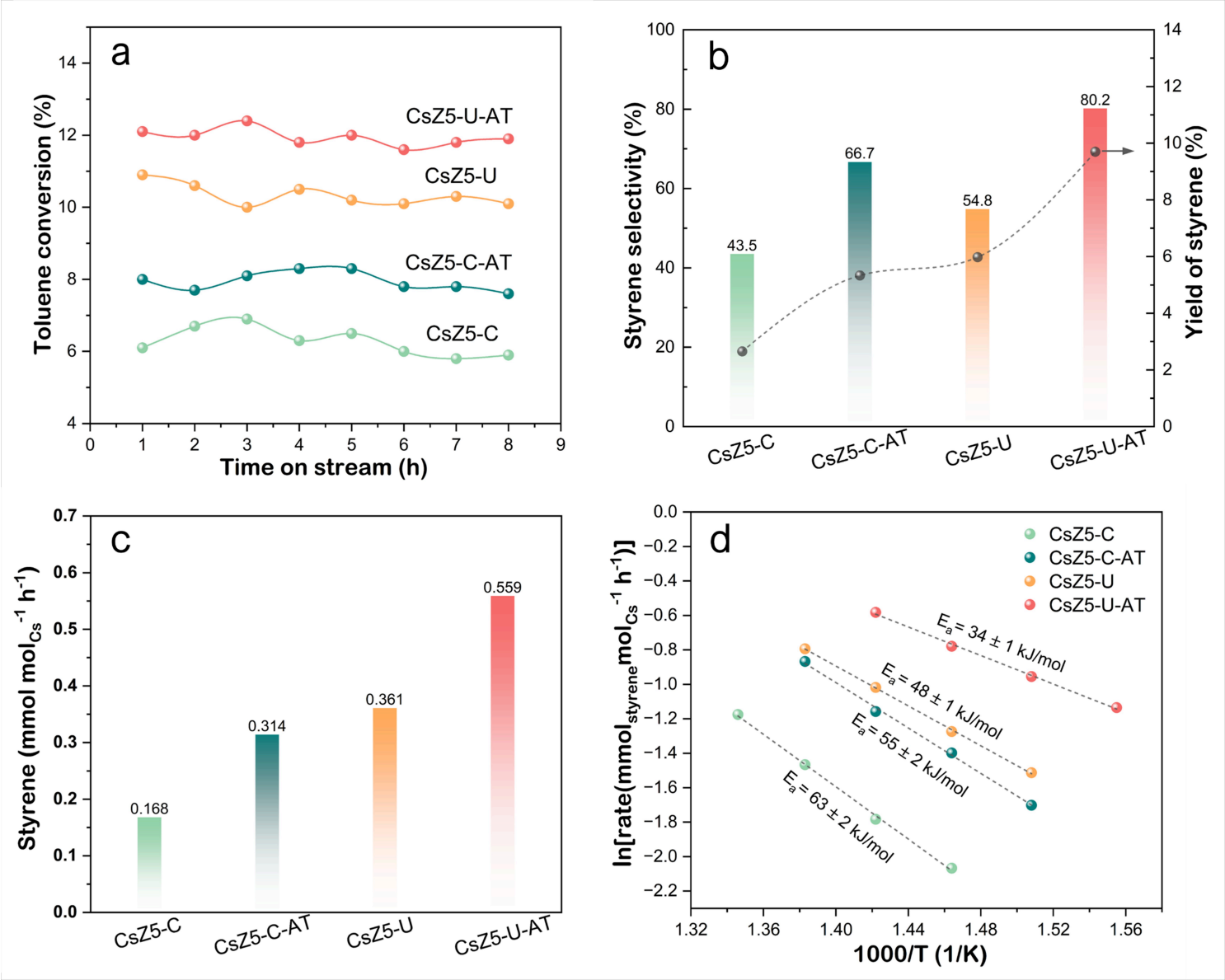


Figure 2

Catalytic performance of various Cs-ZSM-5 catalysts. (a) Toluene conversion. (b) Selectivity and yield of styrene. (c) Normalized reaction rate (mmol$_{ST}$ mol$_{Cs}^{-1}$ h^{-1}). (d) Arrhenius plots versus reaction temperature of different catalysts (370 ^{o}C to 470 ^{o}C). Reaction conditions: 430 ^{o}C, toluene/methanol ratio = 3.0, WHSV = 2.0 h^{-1}.

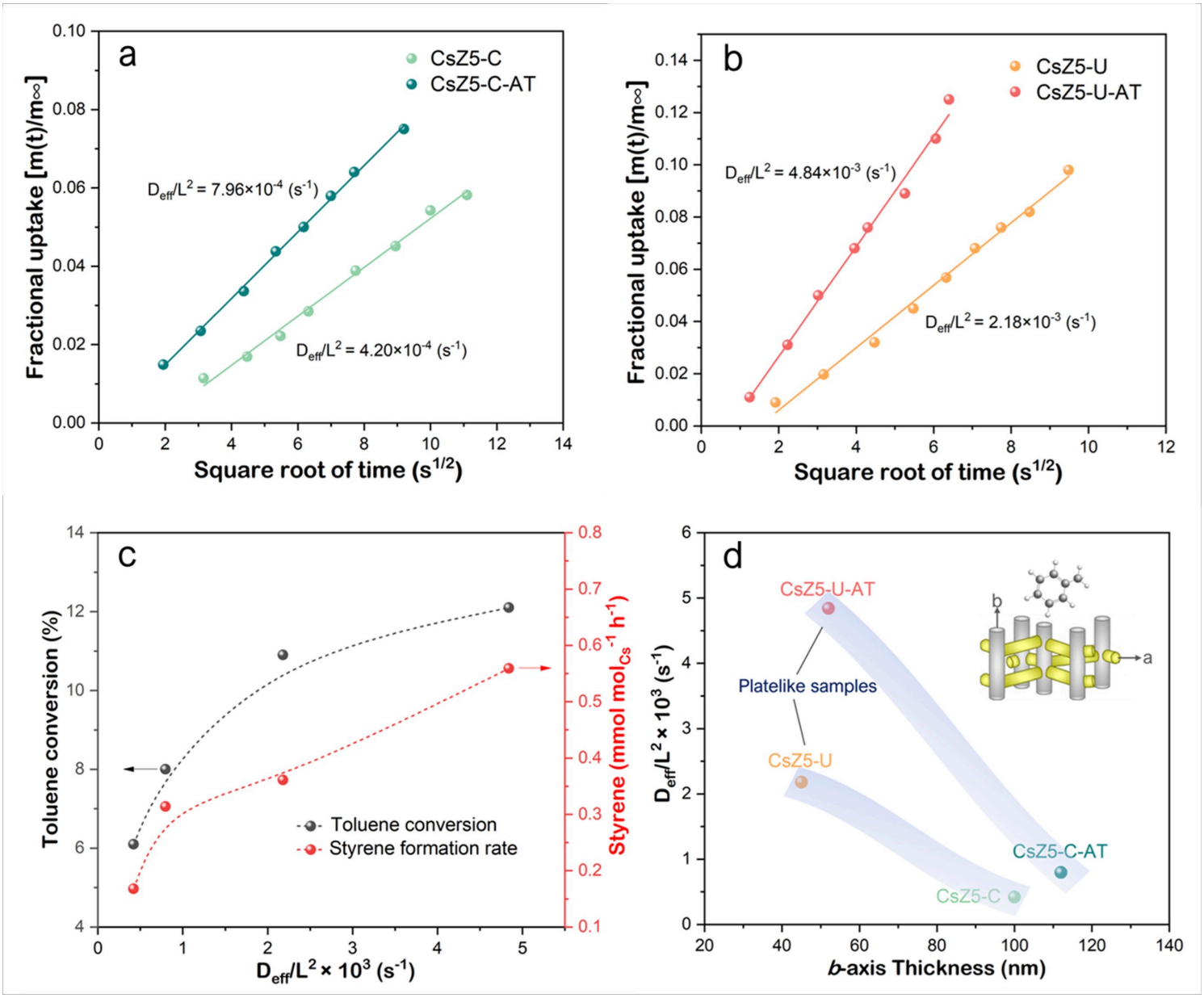


Figure 3

Diffusion behaviors of different Cs-ZSM-5 catalysts. Uptake curves of toluene in (a) CsZ5-C and CsZ5-C-AT, (b) CsZ5-U and CsZ5-U-AT calculated by the IGA technique; (c) Correlation of toluene conversions and styrene formation rates with the diffusion rates of toluene molecules; (d) The relationship between *b*-axis thickness and diffusivity behavior. The detailed conditions of diffusive measurements are displayed in the "**Experimental Procedures**" section.

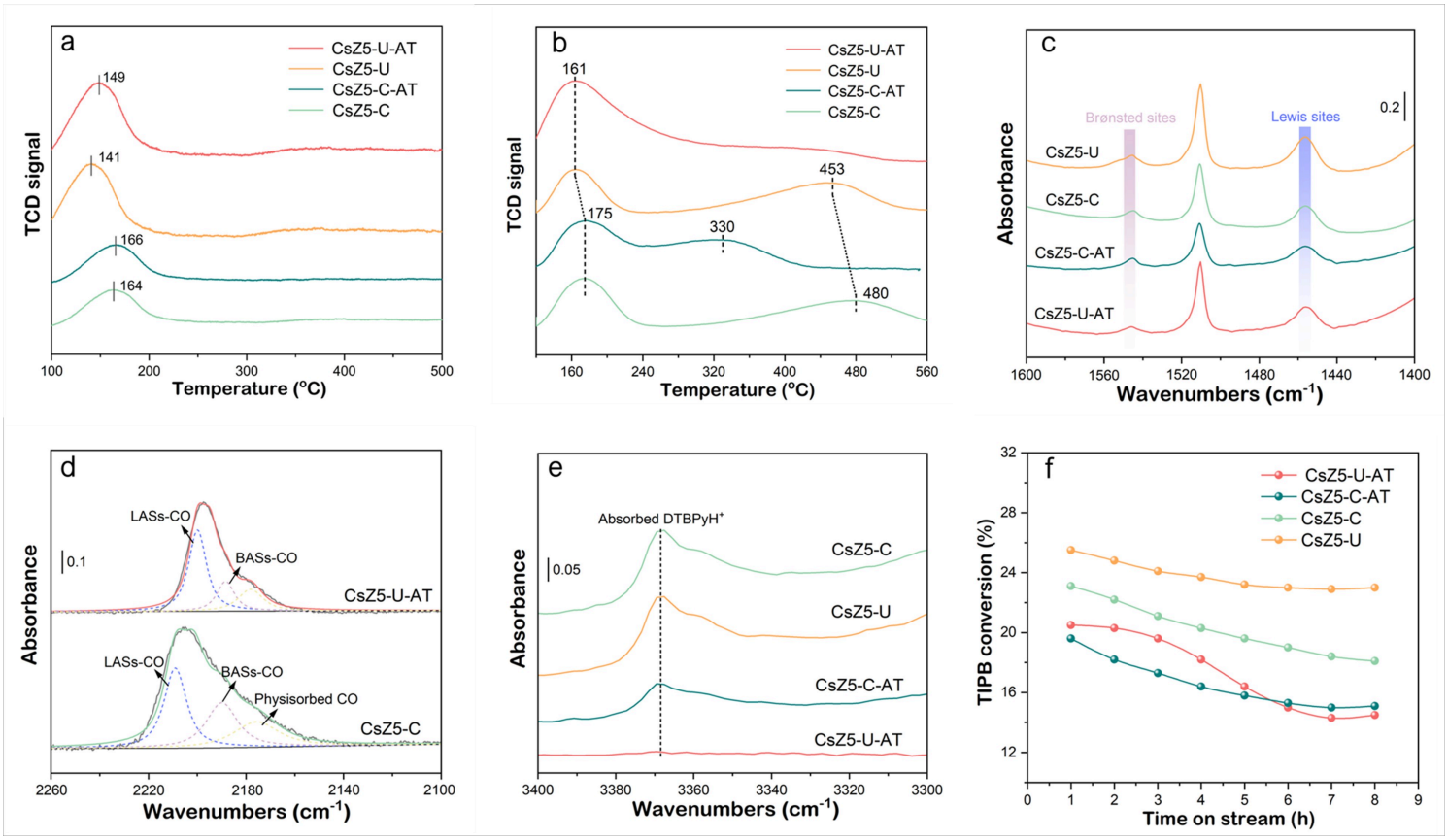


Figure 4

The acid-base properties characterized by different methods. (a) CO_2-TPD profiles; (b) NH_3-TPD profiles; (c) Py adsorbed FTIR spectra with the evacuation temperature of 150 ^oC; (d) CO adsorbed FTIR spectra; (e) DTBPy-adsorbed FTIR spectra at an evacuation temperature of 150 °C; (f) probe reaction for TIPB cracking at 350 ^oC (see detailed reaction conditions in **Supporting Information**).

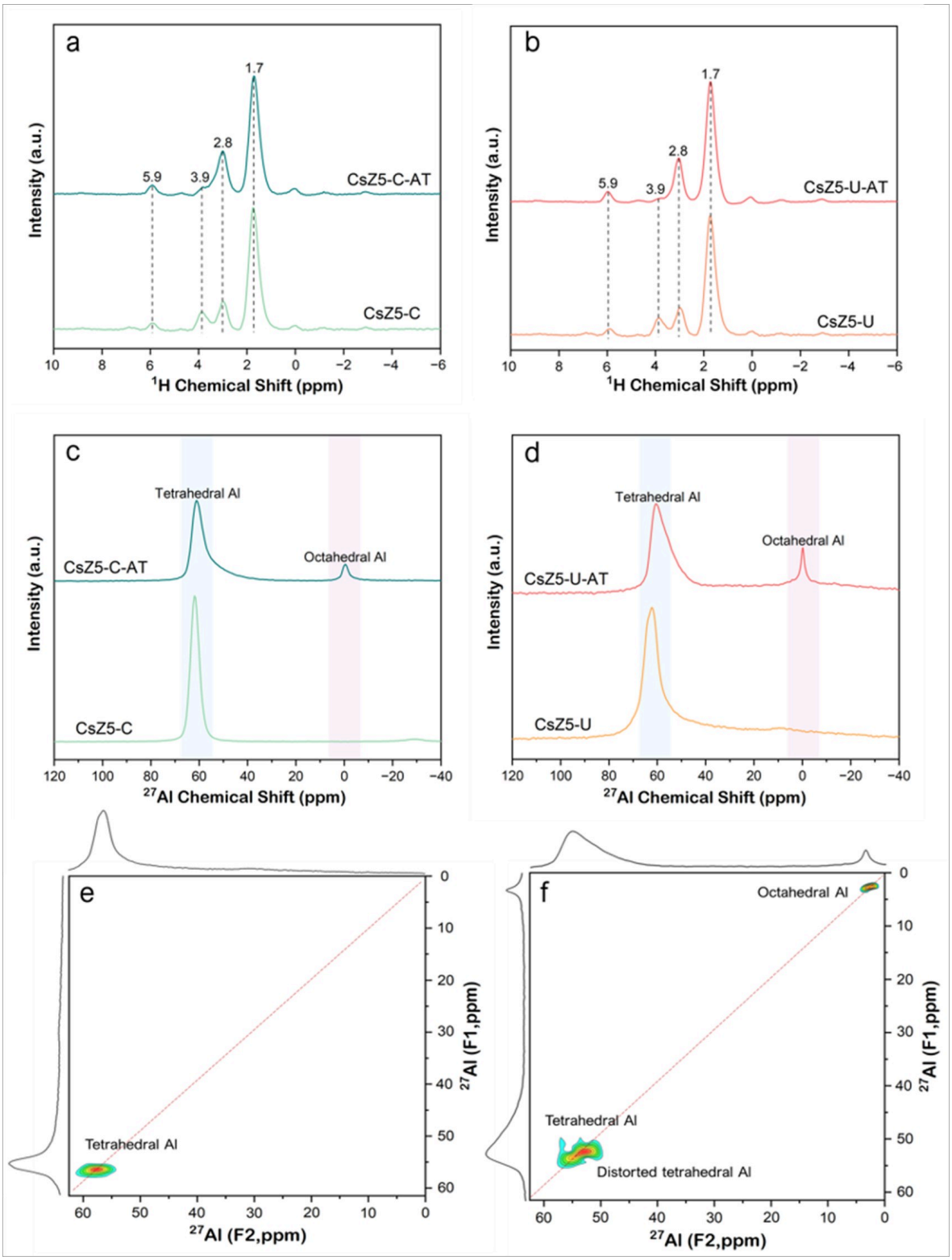


Figure 5

^{1}H MAS NMR spectra of (a) CsZ5-C and alkali-treated CsZ5-C-AT, (b) CsZ5-U and alkali-treated CsZ5-U-AT; ^{27}Al MAS NMR spectra of (c) CsZ5-C and alkali-treated CsZ5-C-AT, (d) CsZ5-U and alkali-treated CsZ5-U-AT; ^{27}Al MQ MAS NMR spectra of (e) CsZ5-U and alkali-treated CsZ5-U-AT.

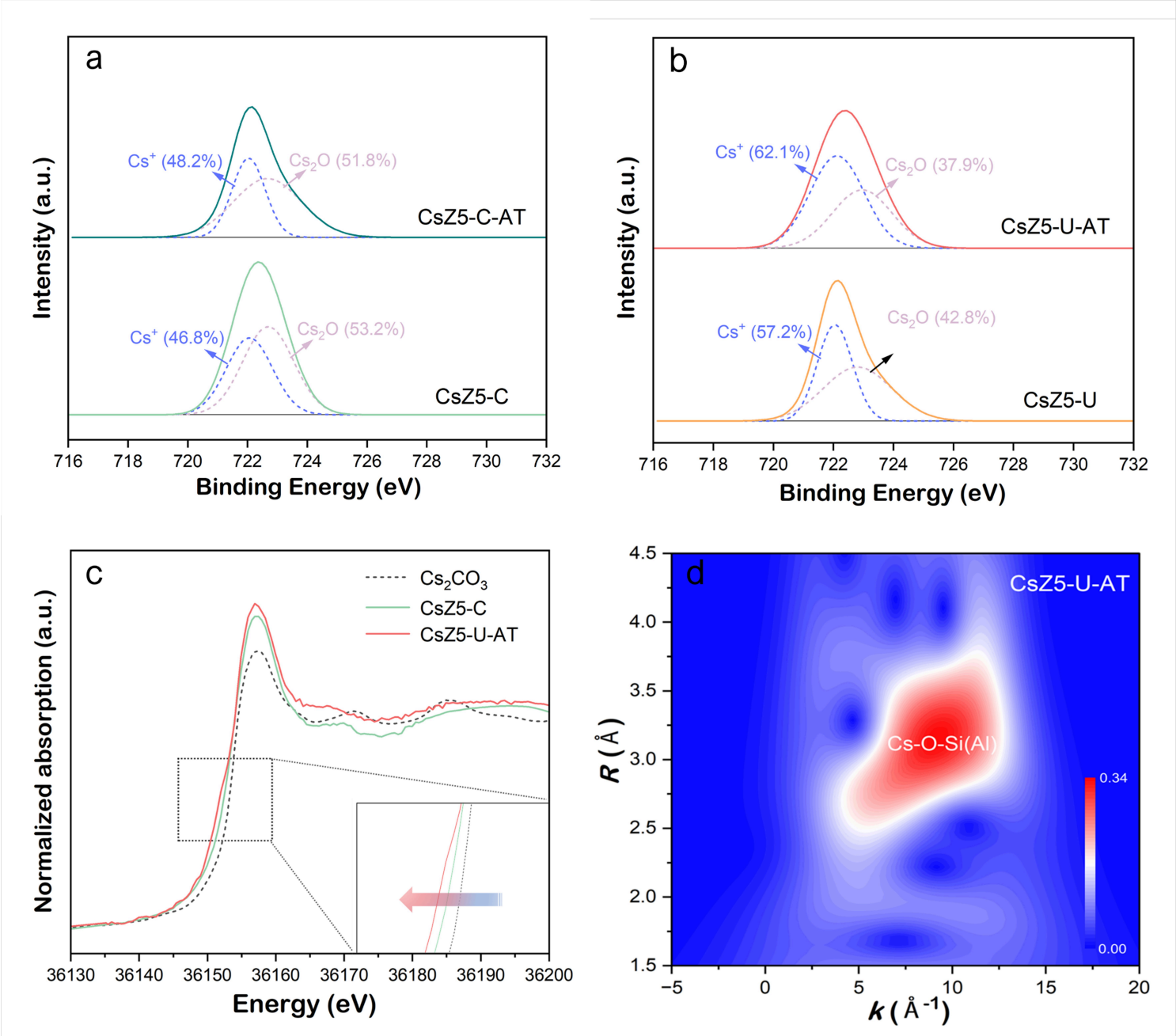


Figure 6

Resolving the chemistry valence states and coordination environment states of Cs Species over different catalysts. (a-b) Cs $3d_{5/2}$ spectra; (c) Cs L_3-edge XANES spectra of CsZ5-C, CsZ5-U-AT and Cs_2CO_3 standard sample; (d) the wavelet transformed (WT) contour plot of the k^3-weighted Cs L_3-edge EXAFS signal for CsZ5-U-AT sample.

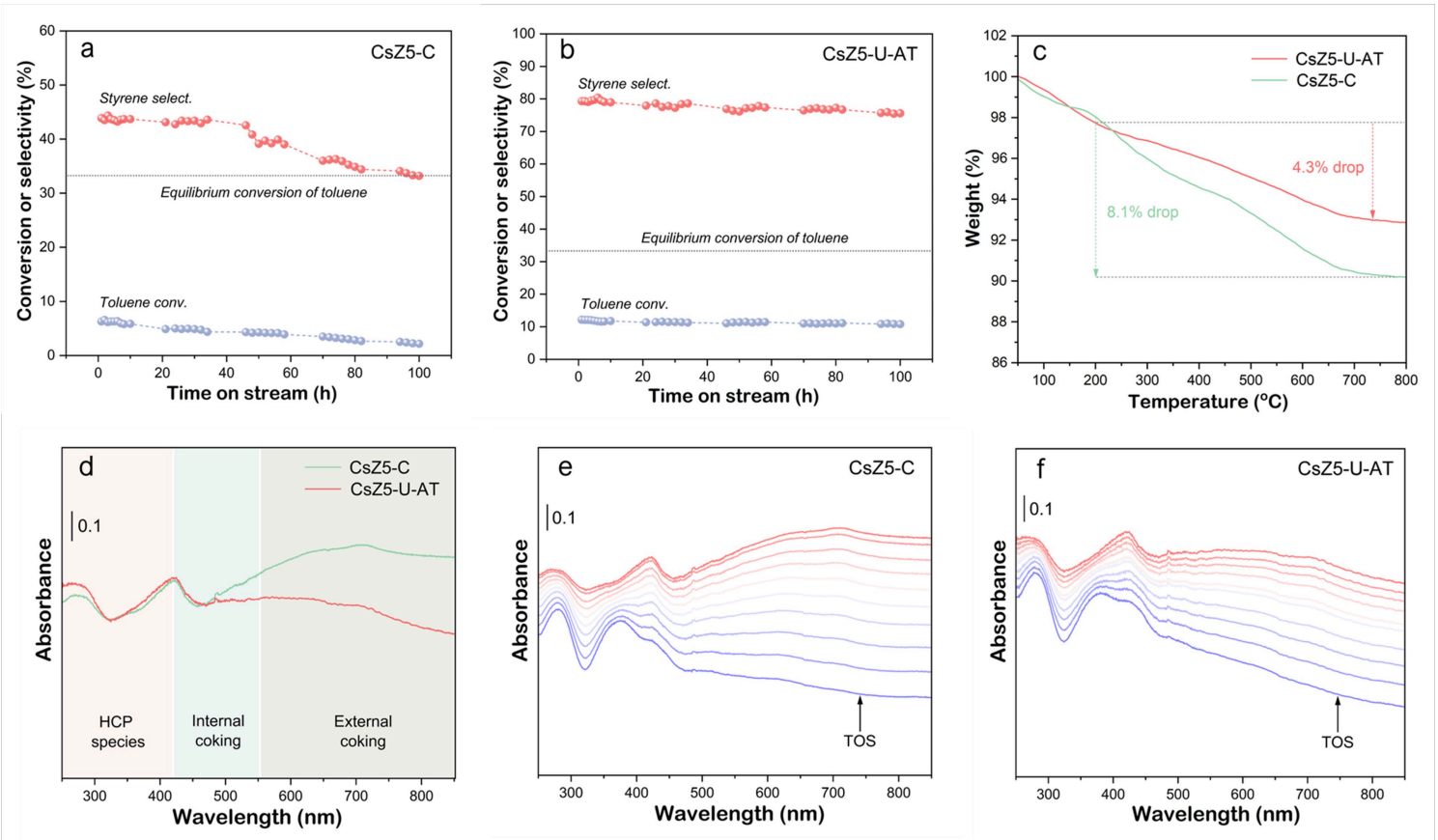


Figure 7

Catalytic stability and the corresponding deactivation mechanism of CsZ5-C and CsZ5-U-AT catalysts. (a, b) Long-time toluene side-chain alkylation test. Reaction conditions: 430^{o}C, toluene/methanol ratio = 3.0, WHSV = 2.0 h^{-1}. (c) TG curves. (d) Operando UV-vis diffuse reflectance spectroscopy after 10 h TOS for CsZ5-C and CsZ5-U-AT at the same reaction conditions. (e, f) Operando UV-vis spectra for CsZ5-C and CsZ5-U-AT collected in 1 h intervals (see **Figure. S20** for data at earlier times within initial 10 min).

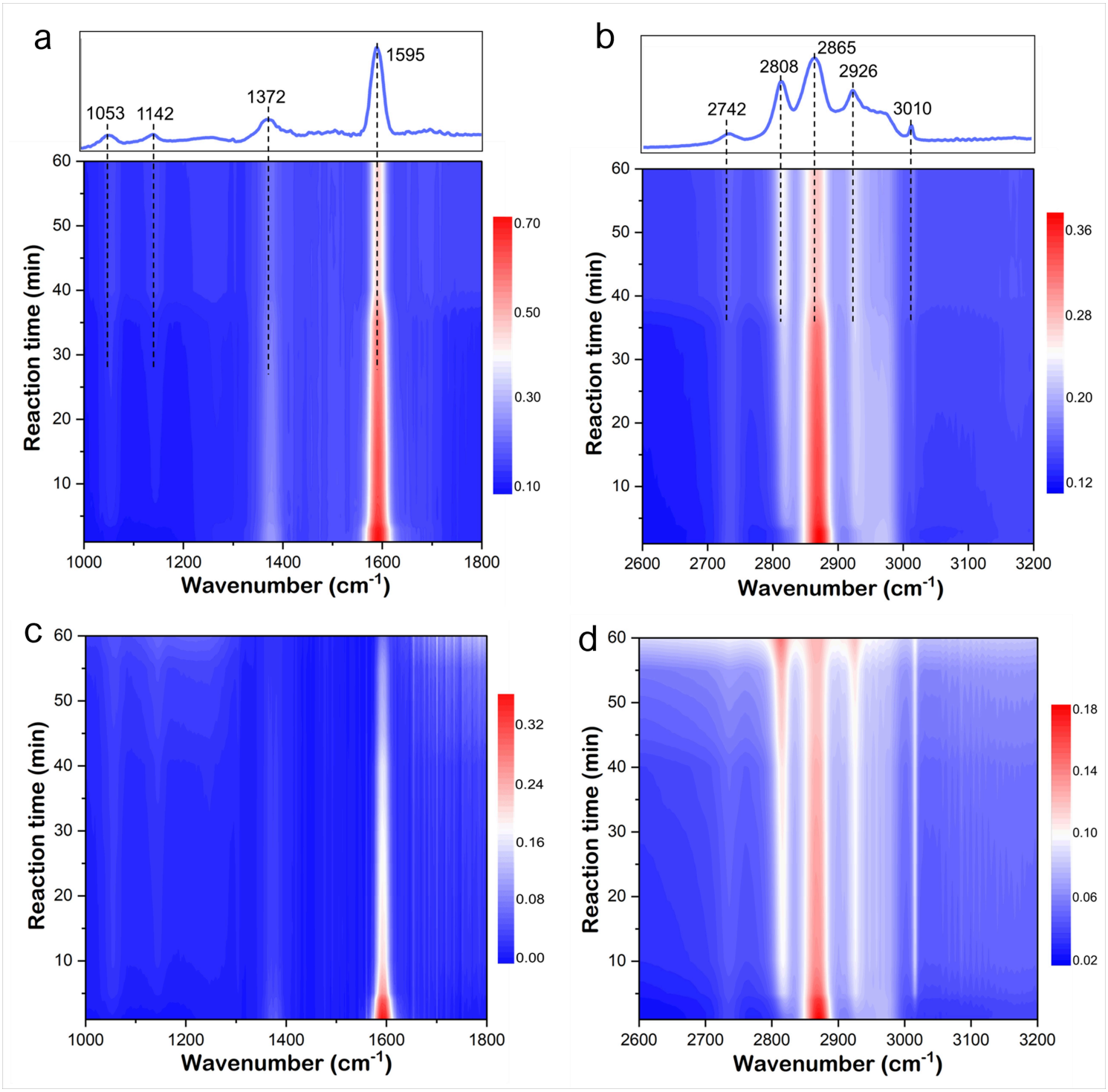


Figure 8

Time-dependent *in situ* DRIFTS from methanol dehydrogenation on (a, b) CsZ5-U-AT and (c, d) CsZ5-C. The spectra were collected from 1 min to 60 min at 430 ^{o}C.

Supplementary Files

This is a list of supplementary files associated with this preprint. Click to download.

- SupportingInformation.docx

- floatimage9.jpeg